AMOC variability and watermass transformations in the AWI climate model

Dmitry Sidorenko[1], S. Danilov[1], Jan Streffing[1], Vera Fofonova[2], Helge Goessling[3], Qiang Wang[1], William David CabosNarvaez[4], Stephan Juricke[5], Nikolay V. Koldunov[1], Thomas Rackow[6], Patrick Scholz[6], Dimitry Sein[1], and Thomas Jung[7]

[1]Alfred Wegener Institute for Polar and Marine Research
[2]Unknown
[3]Alfred Wegener Institute Helmholtz Centre for Polar and Marine Research
[4]University of Alcala
[5]Jacobs University Bremen
[6]Alfred Wegener Institute, Helmholtz Centre for Polar and Marine Research
[7]AWI

November 23, 2022

Abstract

Using the depth (z) and density ( ) frameworks, we analyze local contributions to AMOC variability in a 900-year simulation with the AWI climate model. Both frameworks reveal a consistent interdecadal variability, however the correlation between their maxima deteriorates on year-to-year scales. We demonstrate the utility of analyzing the spatial patterns of sinking and diapycnal transformations through depth levels and isopycnals. The success of this analysis relies on the spatial binning of these maps which is especially crucial for the maps of vertical velocities which appear to be too noisy in the main regions of up- and downwelling because of stepwise bottom topography. Furthermore, we show that the AMOC responds to fast (annual or faster) fluctuations in atmospheric forcing associated with the NAO. This response is more obvious in the than in the z framework. In contrast, the link between AMOC deep water production south of Greenland is found for slower fluctuations and is consistent between the frameworks.

Posted on 23 Nov 2022 — The copyright holder is the author/funder. All rights reserved. No reuse without permission. — https://doi.org/10.1002/essoar.10506856.1 — This a preprint and has not been peer reviewed. Data may be preliminary.

AMOC variability and watermass transformations in the AWI climate model

D. Sidorenko[1], S. Danilov[1,2,3], J. Streffing[2], V. Fofonova[1], H. Goessling[1], Q. Wang[1], W. Cabos[4], S. Juricke[1,2], N. Koldunov[1], T. Rackow[1], P. Scholz[1], D. V. Sein[1,5], T. Jung[1,6]

[1]Alfred Wegener Institute, Helmholtz Centre for Polar and Marine Research, Bremerhaven, Germany.
[2]Department of Mathematics and Logistics, Jacobs University, Bremen, Germany.
[3]A. M. Obukhov Institute of Atmospheric Physics Russian Academy of Science, Moscow, Russia.
[4]Department of Physics and Mathematics, University of Alcala, Alcala, Spain.
[5]Shirshov Institute of Oceanology, Russian Academy of Science, Moscow, Russia.
[6]University of Bremen, Bremen, Germany.

Corresponding author: Dmitry Sidorenko (Dmitry.Sidorenko@awi.de)

Key Points:

- patterns of sinking and diapycnal transformation across depth levels and isopycnals, respectively, can be used to study AMOC variability
- the AMOC subpolar maximum is largely driven by internal transformations
- density framework illustrates the interplay between surface buoyancy flux and interior-mixing

Abstract

Using the depth (z) and density (ϱ) frameworks, we analyze local contributions to AMOC variability in a 900-year simulation with the AWI climate model. Both frameworks reveal a consistent interdecadal variability, however the correlation between their maxima deteriorates on year-to-year scales. We demonstrate the utility of analyzing the spatial patterns of sinking and diapycnal transformations through depth levels and isopycnals. The success of this analysis relies on the spatial binning of these maps which is especially crucial for the maps of vertical velocities which appear to be too noisy in the main regions of up- and downwelling because of stepwise bottom topography. Furthermore, we show that the AMOC responds to fast (annual or faster) fluctuations in atmospheric forcing associated with the NAO. This response is more obvious in the ϱ than in the z framework. In contrast, the link between AMOC deep water production south of Greenland is found for slower fluctuations and is consistent between the frameworks.

Plain Language Summary

In various international programs such as the Climate Model Intercomparison Project (CMIP), climate models are used to study the past, present and future climate. The variability and trends in Atlantic meridional overturning circulation (AMOC) are some of the most important characteristics of an ocean model simulation. Commonly the AMOC is computed as a streamfunction of zonally averaged flow along constant depth levels (z-AMOC). However, there are shortcomings of this approach which are

related to the inclination of density surfaces in the real ocean, which may lead to the appearance of artificial circulation cells. In order to eliminate these artifacts, it is essential to compute the AMOC along constant density surfaces (ϱ-AMOC). That is why recent studies underlined the importance of the ϱ framework for the AMOC analysis. In this paper we analyze the fundamental differences with respect to AMOC variability in both frameworks in a 900-year run with the AWI climate model. We demonstrate that the latitudinal position of overturning maxima, amplitude, and variability show substantial differences between the frameworks. We suggest that the ϱ-AMOC and watermass transformation framework should be used routinely in standard analyses, including forthcoming intercomparison projects.

1. Introduction

The global meridional overturning circulation (MOC) and its Atlantic branch (AMOC) mediate exchanges between the low and high latitudes in the ocean as well as between the hemispheres. The AMOC, which is associated with the formation of dense waters in the North Atlantic, is responsible for a considerable part of global overturning, which makes it an important diagnostic of ocean and climate dynamics (*see, e.g., Kuhlbrodt et al. 2007, Buckley et al. 2016, Johnson et al. 2019*). Given the role of the AMOC in the Earth climate system, there is a special interest in AMOC trends and variability, especially in the context of a changing climate.

Even though several AMOC monitoring programs such as the MOCHA-RAPID array (see, e.g*., Cunningham et al. 2007*) or the Overturning in the Subpolar North Atlantic Program (OSNAP, see, e.g., *Lozier et al. 2019*) have been initiated, model simulations remain crucial for understanding the processes that underlie the AMOC variability. Simulations from ocean models driven by prescribed atmospheric forcing are often used to hindcast the AMOC for intercomparing model performance (e.g., *Danabasoglu et al. 2016*) or to understand the related dynamics such as the role of ocean eddies enhanced by increases in model resolution (see, e.g., *Hirschi et al. 2020*). However, standalone ocean models miss atmosphere-ocean feedbacks which can modulate modes of climate variability such as the Atlantic multidecadal variability (AMV, e.g., *Oelsmann et al. 2020*). That is why AMOC variability must be studied also in coupled atmosphere-ocean models, with transient (historical and future scenario) forcing (including solar, greenhouse-gas, and aerosol forcing) or with constant (e.g., pre-industrial) forcing. The latter has the advantage that models can be run over long temporal scales, which increases the significance of analyses when it comes to understanding internal variability. Furthermore, analyses of AMOC variability in coupled models can shed light on important interactions in the climate system.

Along these lines, *Danabasoglu et al. 2012* analyzed the AMOC variability in CCSM4. The authors showed that various AMOC index time series tend to lead sea surface temperature (SST) changes in high latitudes and thus confirmed the driving role of the AMOC. Similar results were obtained by *Frankignoul et al. 2013* based on

CCSM3. Using 10 climate models, *Roberts et al. 2013* identified a link between the trend in the AMOC at 26.5°N and subsurface density anomalies in the Subpolar Gyre while finding large spread in patterns and magnitudes of SST response. *Ortega et al. 2012* analyzed two IPCC scenarios and the last-millenium run in ECHO-G. They found that AMOC variability at different frequencies is controlled by different processes: high frequencies are associated with local changes in Ekman transport caused by multiple modes of atmospheric variability, whereas low frequencies are linked with deep-water production south of Greenland. Xu et al. 2019 analyzed 44 CMIP5 climate simulations and 18 standalone ocean simulations, finding no robust link between the AMOC and the North Atlantic Oscillation (NAO) in CMIP5, in contrast to a stronger link in standalone ocean runs. However, they found a strong link between the deep water production in the western subpolar North Atlantic and the AMOC also in the CMIP5 simulations. *Menary et al. 2013, 2020a* described the mechanisms of aerosol- forced AMOC variability in the Hadley Centre Global Environment Model 2. Using the same model, the recent work by *Menary et al. 2020b* reconciled the modelled and observational OSNAP data and demonstrated that the Labrador Sea may not be the origin of AMOC variability although it correlates with the densities there. Even though tremendous progress in understanding AMOC variability has been made over the past years, model results appear to be dependent on model uncertainties and resolution (see, e.g., *Katsman et al., 2018; Menary & Hermanson, 2018; Reintges et al. 2017*; *Xu et al. 2019, Menary et al. 2020b*).

There are two caveats in existing studies inquiring into the AMOC variability in the climate system. First, many studies still consider AMOC as a function of depth and latitude (z-AMOC), whereas AMOC as a function of density and latitude (ϱ-AMOC) might be a more appropriate diagnostic (*see, e.g., Zhang et al. 2010, Kwon et al. 2014, Johnson et al. 2019, Sidorenko et al. 2020a*). Indeed, ϱ-AMOC is directly connected to surface water-mass transformations, which are simply its constituent part (e.g., *Walin 1982, Xu et al. 2018*). The other part comes from internal transformations (see, e.g., *Xu et al. 2018, Sidorenko et al. 2020a*). The latter are mainly due to horizontal and vertical mixing, and partly due to the nonlinearity of the equation of state. In this respect, ϱ-AMOC explicitly reveals the roles of surface and internal transformations in sustaining AMOC variability, as discussed in *Grist et al. 2009*. *Zhang et al. 2010* and *Kwon et al. 2014* explicitly mention the need in studying ϱ-AMOC for the understanding of the processes in subpolar latitudes. However, AMOC computation in density space is less straightforward and requires either high-frequency model output or online computations, which is rarely done. Hence, AMOC computations in density space are often compromised by using low-frequency output which varies from several days (see, e.g., *Megann et al. 2018*) to one month (see, e.g., *Kwon et al, 2014*). This may bias the diagnostics when mesoscale processes come into play. The second caveat is related to the fact that the AMOC represents the net effect from processes happening at different locations. While numerous studies try to correlate variability in physical processes with that of the

AMOC, the direct analysis of sinking through an appropriate depth level, or diapycnal transformation through the isopycnal that corresponds to the center of the main AMOC cell, is much more revealing (*e.g., Xu et al. 2018, Sidorenko et al. 2020a*). Such an analysis shows which locations are the main contributors to AMOC variability, and helps to judge the physics of processes that are involved.

The main goal of this paper is to understand local contributions to AMOC variability simulated in a new climate model, AWI-CM, by comparing the z- and density frameworks. Its secondary goal is to draw attention to the utility of local analyses of sinking or water-mass transformations that constitute the AMOC when integrated over constant depth or density surfaces respectively. To this end we analyze the output of a pre-industrial AWI-CM run over a period of 900 years. The water-mass transformations are diagnosed online during the model simulation (*Sidorenko et al. 2020a*). We analyze not only the z- and ϱ-AMOC streamfunctions and their index timeseries, but also the spatial patterns of sinking and density transformations through depth levels and isopycnals.

The paper is organized as follows: Section 2 describes the model simulation. Section 3 introduces the density and depth frameworks for AMOC computation. Section 4 addresses the variability of both AMOCs and the associated climate patterns and mechanisms. The last two sections present the discussion and conclusions.

2. Model simulation

A pre-industrial control simulation (PIC) was generated with the AWI climate model (AWI-CM Sidorenko et al., 2015, Rackow et al., 2016, Sidorenko et al., 2019) which is built upon Finite-volumE Sea ice–Ocean Model (FESOM 2.0; Danilov et al., 2004; Wang et al, 2008; Timmermann et al., 2009; Wang et al, 2014, Danilov et al. 2015, Scholz et al. 2019) and is available with several atmospheric components in climate setups. Here FESOM was run in combination with OpenIFS (cycle 43), the atmosphere model developed at ECMWF. This new climate configuration will be described more extensively in a separate paper. AWI-CM was run under pre-industrial forcing for 1000 years and the last 900 years were used for the analysis presented.

FESOM was set up at a resolution which varies from nominal one degree in the interior of the ocean to 1/3 degree in the equatorial belt and 24 km (1/4 degree meridionally) north of 50°N. The ocean surface is discretized with about 127,000 grid points, and 46 vertical levels are used. This mesh has been used in the CORE-II model intercomparison project (e.g., Wang et al. (2016a,b)) and Ocean Model Intercomparison Project phase 2 (OMIP-2, Tsujino et al., 2020). OpenIFS was used in TCO159 configuration (reduced Gaussian triangular– cubic-octahedral grid truncated at wave number 159 spectral resolution).

The algorithms for the AMOC computation on unstructured meshes are described in *Sidorenko et al. (2020a,b)*. Here we calculated the transports in density space during run time, which overcomes the need of large storage of almost all previous work that has used this kind of analysis (*see eg. Megann (2018)*).

The ϱ bins are chosen according to *Megann (2018)* (72 levels for a good representation of deep and bottom waters), complemented with additional density levels to include those presented in *Xu et al. (2018)*. Altogether we use 85 density bins spanning the range of $30.0 < \varrho < 37.2$ kg m^{-3}.

3. AMOC frameworks

The AMOC derived in the two different frameworks is presented in Figure 1. The traditional computation in depth coordinates, referred to as z-AMOC, is characterized by a mid-depth cell centered at ~1000 m and a bottom cell centered at ~4000 m. The maximum of the mid-depth cell is located at ~40°N. It is several degrees south of the main regions of deep convection, which is typical for the depth representation in coarse-resolution runs. The region of closed streamlines around the AMOC maximum, including the diagnosed upwelling slightly south of the maximum, is referred to as recirculation cell. In Fig. 1 (left panel) it is confined between 50°N and 30°N and is similar to that in the standalone FESOM configuration described in *Sidorenko et al. 2020a*. The authors attribute a part of this recirculation on coarse meshes to spurious numerical mixing and demonstrate that it can be significantly reduced if a higher model resolution is used.

The left panel in Fig. 3 depicts the vertical velocity at 1000m which has been conservatively remapped onto a 4°x4° grid prior to plotting. On the original mesh the vertical velocity exhibits a noisy structure which masks the main signal. This structure is the consequence of stepwise bottom representation and does not disappear with spatial averaging (see patterns in *Katsman et al. 2018*). Similar to *Sidorenko et al. 2020a* the above-mentioned recirculation cell is caused by the downward flux in the Gulf Stream region and in the Eastern North Atlantic, and the upward flux at Cape Hatteras.

AMOC in density space Fig. 1 (right panel), referred further to as ϱ-AMOC, has a mid-depth cell located at ϱ=36.7 kg m^{-3} and a less expressed bottom cell at ϱ=37 kg m^{-3}. The maximum of the mid-depth cell, as opposed to z-AMOC, is found at ~55°N which is close to the regions of deep convection. The associated recirculation is confined between 40°N and 65°N, similar as in other studies (*e.g., Sidorenko et al. 2020a, Xu et al. 2018*). The diapycnal velocity across ϱ=36.65 kg m^{-3} is presented in Fig.2 (right panel). The buoyancy loss (density increases) associated with the ϱ-AMOC increase is found in a zonal band between ~60°N and ~65°N. The recirculation is closed by buoyancy gain (density decreases) which takes place within the Gulf Stream and along the route of the North Atlantic Current (NAC).

The surface-forced diapycnal water mass transformation (Ψ_s) and the interior transformation (Ψ_I) are shown in Fig. 3 (see *Sidorenko et al. 2020a,b* for computation details). Ψ_s is characterized by three main cells which are all within the upper limb of the AMOC and their difference mostly reflects the fact that they are in different latitudinal circulation regimes. The three cells are centered at ϱ=30.95 kg m^{-3}, ϱ=36.52 kg m^{-3} and ϱ=36.89 kg m^{-3}. The maximum of Ψ_I (~15Sv) is found at 55°N and indicates that the recirculation cell in ϱ-AMOC is largely maintained through internal transformations. It is, however, found at slightly higher densities ϱ=36.77 kg m^{-3} (compared to ϱ=36.7 kg m^{-3} for the maximum of ϱ-AMOC), which also highlights the role of Ψ_s.

One of the prominent differences between the two frameworks is the location of the AMOC maxima which is found at different latitudes. While both frameworks show predominant sinking and buoyancy loss north of 55°N and upwelling and buoyancy gain at the Gulf Stream separation area near Cape Hatteras, there is no coherent signal found at the interface between the subtropical and subpolar gyres. There the diapycnal velocity along the NAC acts towards buoyancy gain and contributes to the decrease of ϱ-AMOC, defining the southern end of the recirculation cell. From inspecting Ψ_s and Ψ_I in Fig. 3 we may conclude that the NAC front is characterized by large internal transformations taking place below ϱ=36.7 kg m^{-3}. Concurrently, vertical velocity depicts sinking along the NAC and marks the northern end of the recirculation cell in z-AMOC. The sinking is associated with the inclination of isopycnals at the boundary of the gyres where the along-isopycnal flow allows for non-zero vertical component in z representation. Hence, the position of the NAC matches the latitude where ϱ=36.7 kg m^{-3} starts to flatten at a depth of ~1000m towards the south, remaining largely flat south of 30°N (not shown).

In general, we find that the mean AMOC in both frameworks in our coupled model simulation looks qualitatively similar to those in ocean-alone simulations (e.g., Sidorenko et al. 2020a, Xu et al. 2018). The fact that the AMOC maxima are found at different latitudes in the two frameworks points to differences in the underlying mechanisms. One would expect that using ϱ-AMOC is physically more appealing as it directly accounts for water mass transformations between different density classes (e.g., *Johnson et al. 2019, Sidorenko et al. 2020a*).

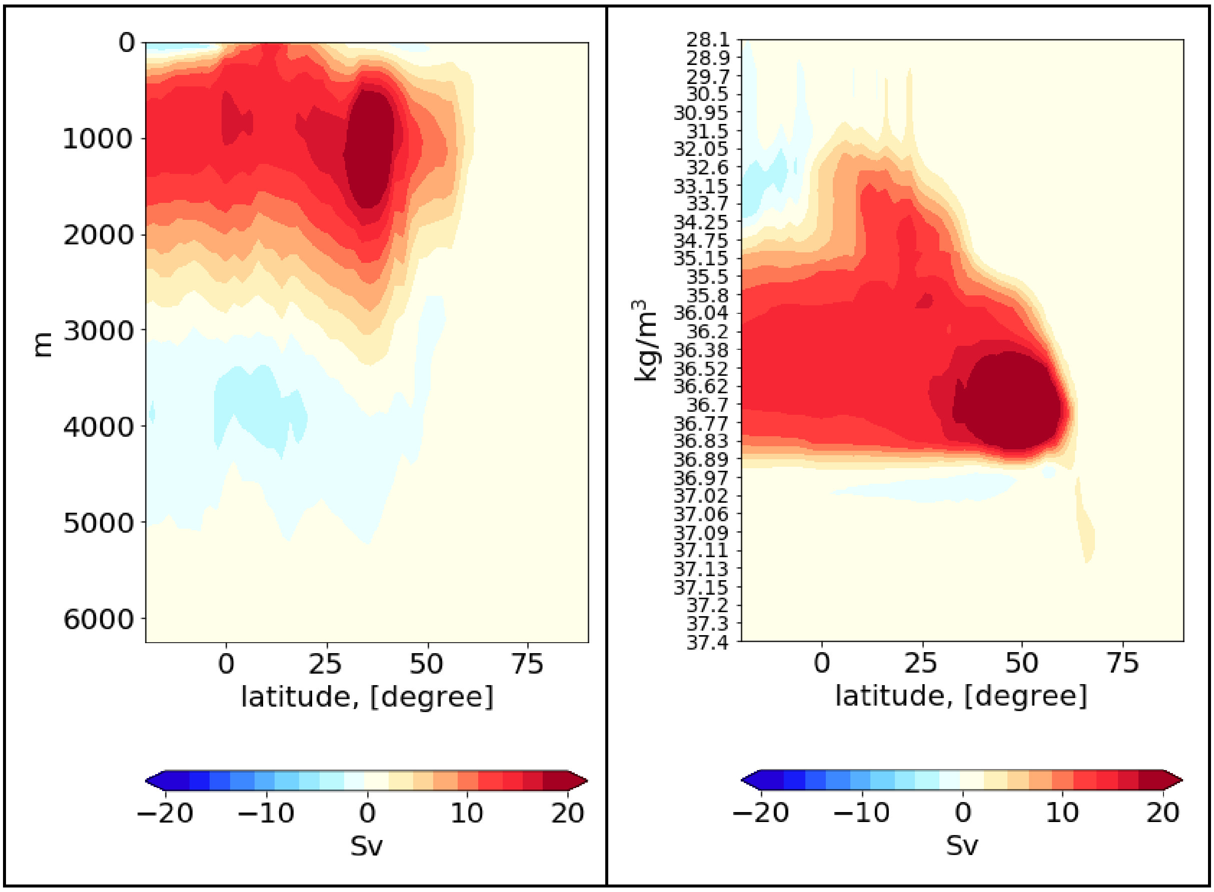

Figure 1: mean z-AMOC (left) and ϱ-AMOC (right) averaged over 900 years of the model run.

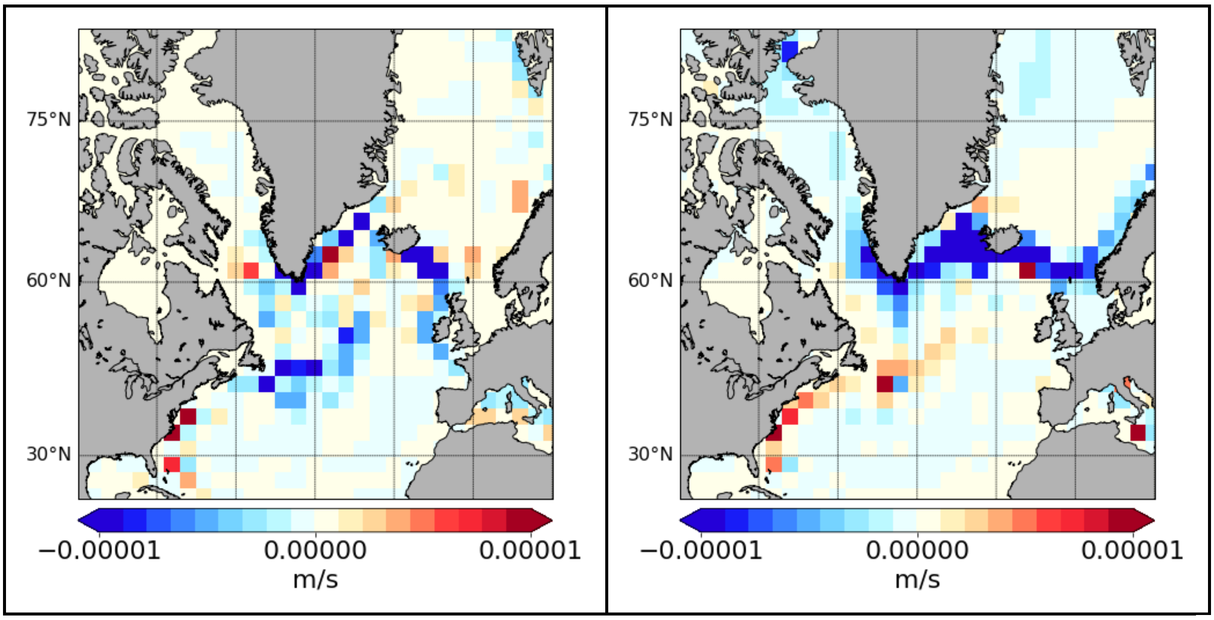

Figure 2: 900-year mean vertical velocity at 1000 m (left) and diapycnal velocity at ϱ=36.7 kg/m^3 (right), conservatively remapped onto a 4°x4° grid.

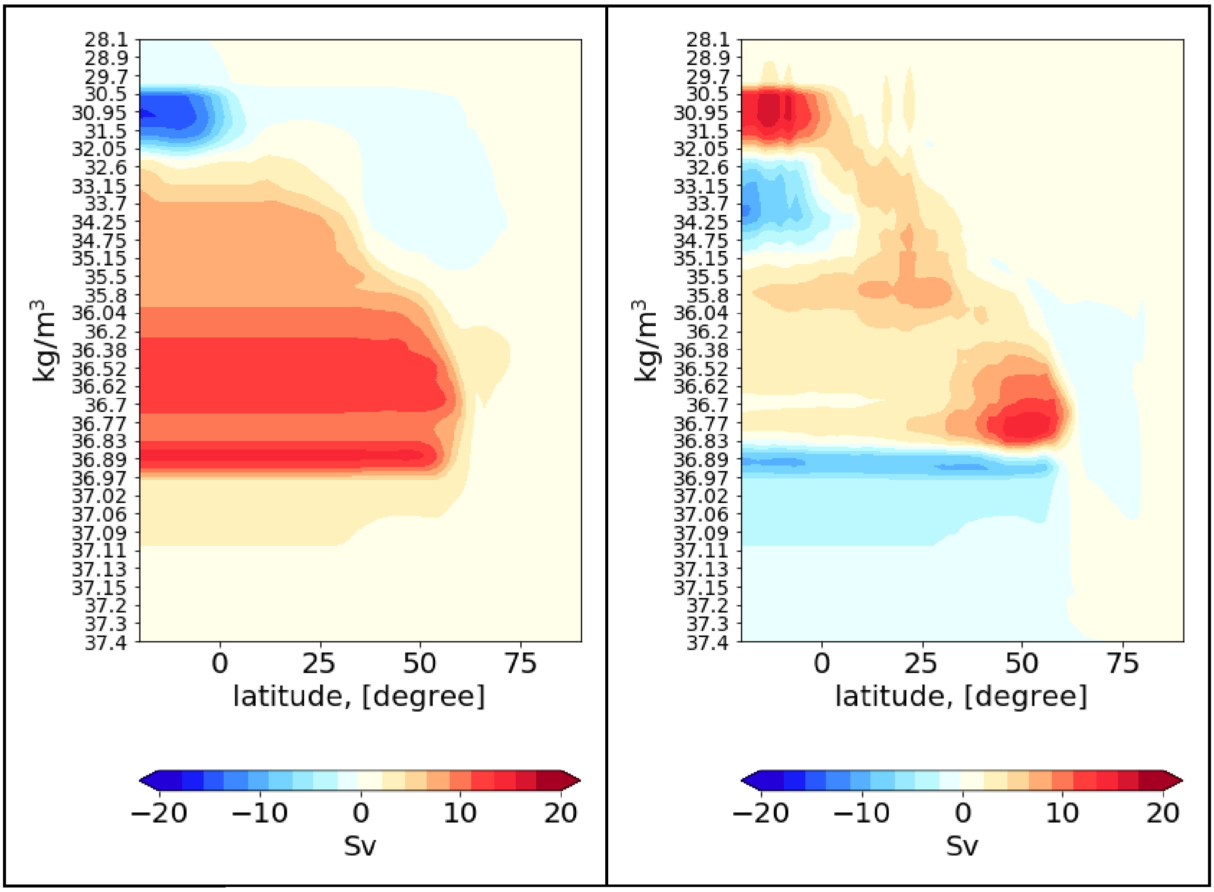

Figure 3: Left: surface-forced diapycnal transformations (Ψ_S) as a function of latitude and density. Right: interior-mixing-induced transformations (Ψ_I).

4. AMOC variability

4.1 Subtropical and subpolar maxima

Traditionally the AMOC variability is quantified with the timeseries of the streamfunction maximum at a certain latitude. In some studies the timeseries of the subtropical AMOC maximum is used. There the latitude is often chosen to be either 30°N, where the AMOC matches the center of the overturning cell (see eg. Reintges et al. 2017), or 26.5°N, the location of the observational MOCHA-RAPID array (*e.g., Cunningham et al. 2007*). Other works address the subpolar AMOC, which is often computed at 40°N-45°N, at the location of the z-AMOC maximum. The subtropical and subpolar variabilities differ in amplitude, are lagged with each other by some years and may poorly correlate at year-to-year timescales. In our simulation, the largest variability is found for the subpolar AMOC at the locations of respective maxima. As we have shown above, the location of subpolar maxima for depth and density frameworks in our experiment are at ~40°N and ~55°N, respectively. The standard deviations of the AMOC maxima reach 1.33Sv in z-AMOC and 1.68Sv in ϱ-AMOC. At 30°N a smaller variability is detected with a standard deviation of 0.93Sv in both frameworks. This indicates that, although the sinking and diapycnal transformations defining AMOC are largely located in the northern North Atlantic, only a part of this variability is communicated with the subtropical AMOC. This implies that significant transformations take place between subtropical and subpolar regions.

The variability of the subpolar AMOC maxima is shown in Fig. 4 (upper panel). The time-averaged maximum of the ϱ-AMOC is ~25.9Sv and is larger than that of the z-AMOC (~24.0Sv). The correlation between both frameworks at year-to-year timescale is only ~0.34 for 0-lag. It is symmetric about 0-lag and increases to 0.47 for ±1-lag and then drops to 0.1 already at ±4-lag. This is an interesting result, illustrating that not only the subpolar maximum and its position but also the variability is affected by the choice of framework.

The variability of the subtropical AMOC maxima is shown in Fig. 4 (bottom panel). The correlation between both frameworks is 0.98. This reflects the fact that the density surface is nearly flat across the basin south of 30°N and both frameworks coincide. This also agrees with the findings by Zhang et al. 2010 who studied the latitudinal dependence of AMOC in both frameworks.

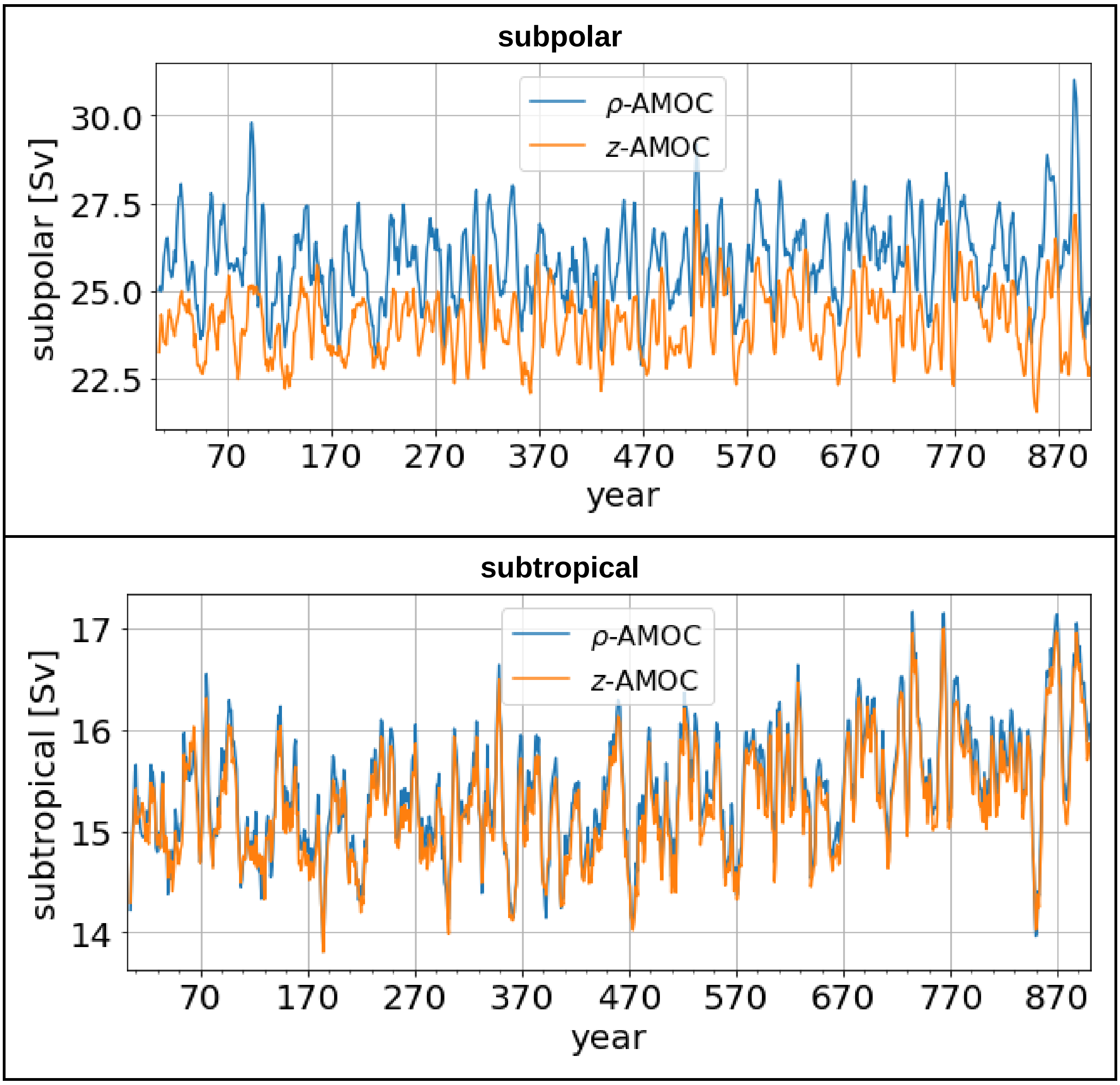

Figure 4: Annual mean time series of the subpolar (above) and subtropical (bottom) AMOC maxima in z and ϱ representations. Subtropical AMOC is computed at 30°N. Subpolar AMOC is computed as AMOC maxima north of 40°N and is located at ~40°N in z and at ~55°N in ϱ frameworks, respectively. Both maxima have been computed within the entire depth (density) range. For visualisation, a 5-year moving average has been applied to the timeseries prior to plotting.

4.2 AMOC composites

Differences between composite patterns of AMOC anomalies computed for the periods of high (AMOC$^+$) and low (AMOC$^-$) values of subpolar AMOC maxima are shown in Fig. 5 for the two frameworks. Events where the AMOC deviates from the mean by more than one standard deviation have been considered. The spatial pattern in the z framework is expressed by a recirculation cell of ~6Sv centered at ~40°N within the upper 4000m. In contrast, the spatial pattern in ϱ framework is expressed by two cells which highlight the difference in associated processes within the light and heavy density classes. The positive cell is centered at 55°N within the density range 35.8 kg $m^{-3}<\varrho<36.97$ kg m^{-3} and has a similar maximum value of ~6Sv. The negative cell starts east of the positive one within the narrow density range 36.83 kg $m^{-3}<\varrho<36.97$ kg m^{-3} and has a minimum of -3Sv at ~40°N. Its spread over a large latitudinal range points to the role of the fluctuations in volume below respective isopycnals during ϱ-AMOC$^+$ and ϱ-AMOC$^-$ phases. For obtaining annual-mean density transformations this motion of isopycnals shall be subtracted from the total signal. Since the present study was initially meant for AMOC and not transformation analysis, these data have not been stored. Therefore, what we address below as total and internal transformation might be affected by the motion of isopycnals. Yet, the inconsistency was verified not to cause any impact onto the presented results. We address this issue later in the discussion section.

Fig. 6 shows the difference between composite patterns of surface buoyancy forced ($\square\Psi_s$) transformations for different lags (in years) with respect to the subpolar ϱ-AMOC index. For the negative lags (Ψ_s leads) we observe positive anomalies which are confined between 36.7 kg $m^{-3}<\varrho<$ and 36.97 kg m^{-3} south of 55°N. This indicates that the surface forcing acts to reduce the buoyancy of this density range. At lag 0, when the AMOC reaches its maximum, and thereafter the pattern is reversed, indicating a decrease in buoyancy of water with densities $\varrho>36.7$ kg m^{-3}. Concurrently, the dipole anomaly centered at 36.89 kg m^{-3} (most expressed at lags 0 and 2) points to the shift of the respective deep water production cell (seen as a bottom cell in Fig. 3, left) towards lighter densities.

Neglecting the model drift and the motion of isopycnals one could write $\square\Psi_\varrho=\square\Psi_s+\square\Psi_I$. In Fig. 7 we show the annual maps for $\square\Psi_I$ at different lags. Note that the sum of $\square\Psi_I$ and $\square\Psi_s$ at lag 0 will equal to the signal in the right panel in Fig. 5. Comparing $\square\Psi_I$ and $\square\Psi_s$ reveals that $\square\Psi_s$ alone explains only a small portion of variability in ϱ-AMOC, especially at lag 0. Furthermore, surface transformations affect the variability of ϱ-AMOC in the density classes which are far larger than the density at which the ϱ-AMOC maximum is located. Thus the interior-mixing-induced transformations are not only responsible for the existence of the mean recirculation in ϱ-AMOC, forming its subpolar maximum, but also for its variability. This highlights the importance of the interplay between surface buoyancy flux and interior-mixing in the higher density classes.

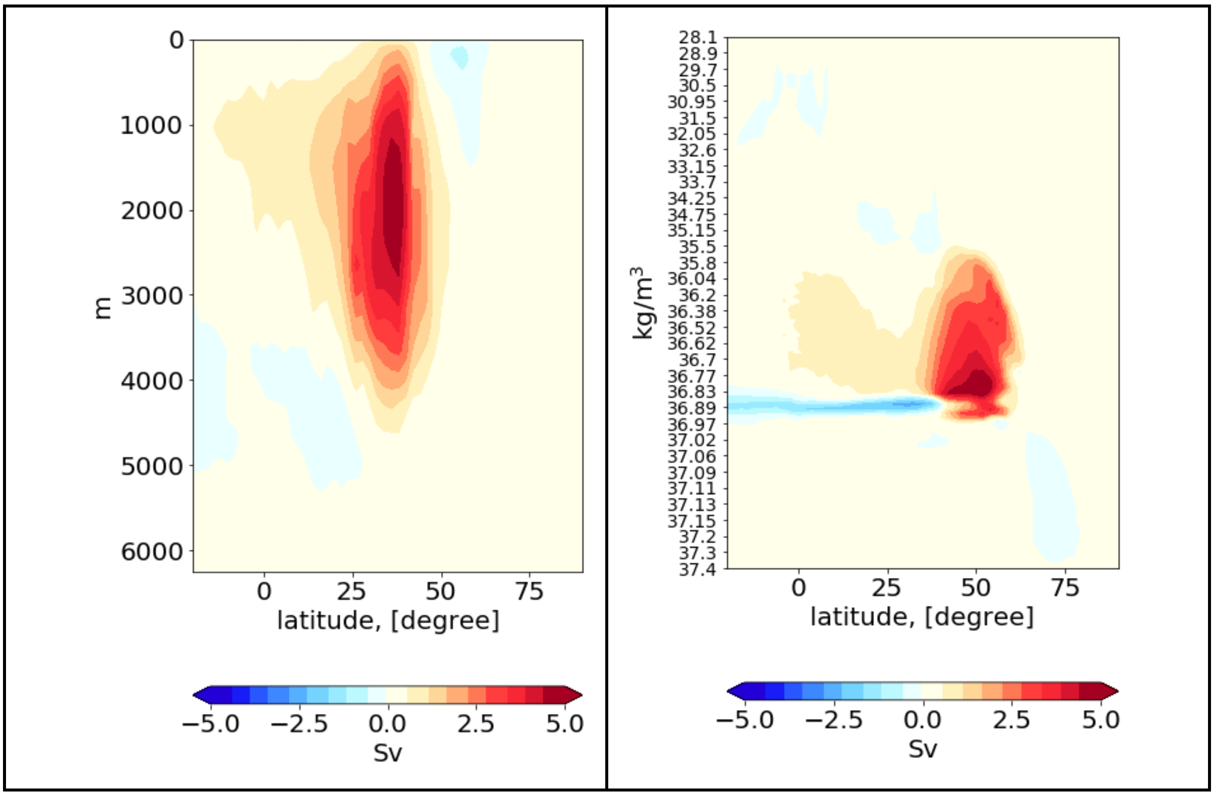

Figure 5: Differences between supbpolar AMOC^{+} and AMOC^{-} composite patterns of z-AMOC (left) and ϱ-AMOC (right).

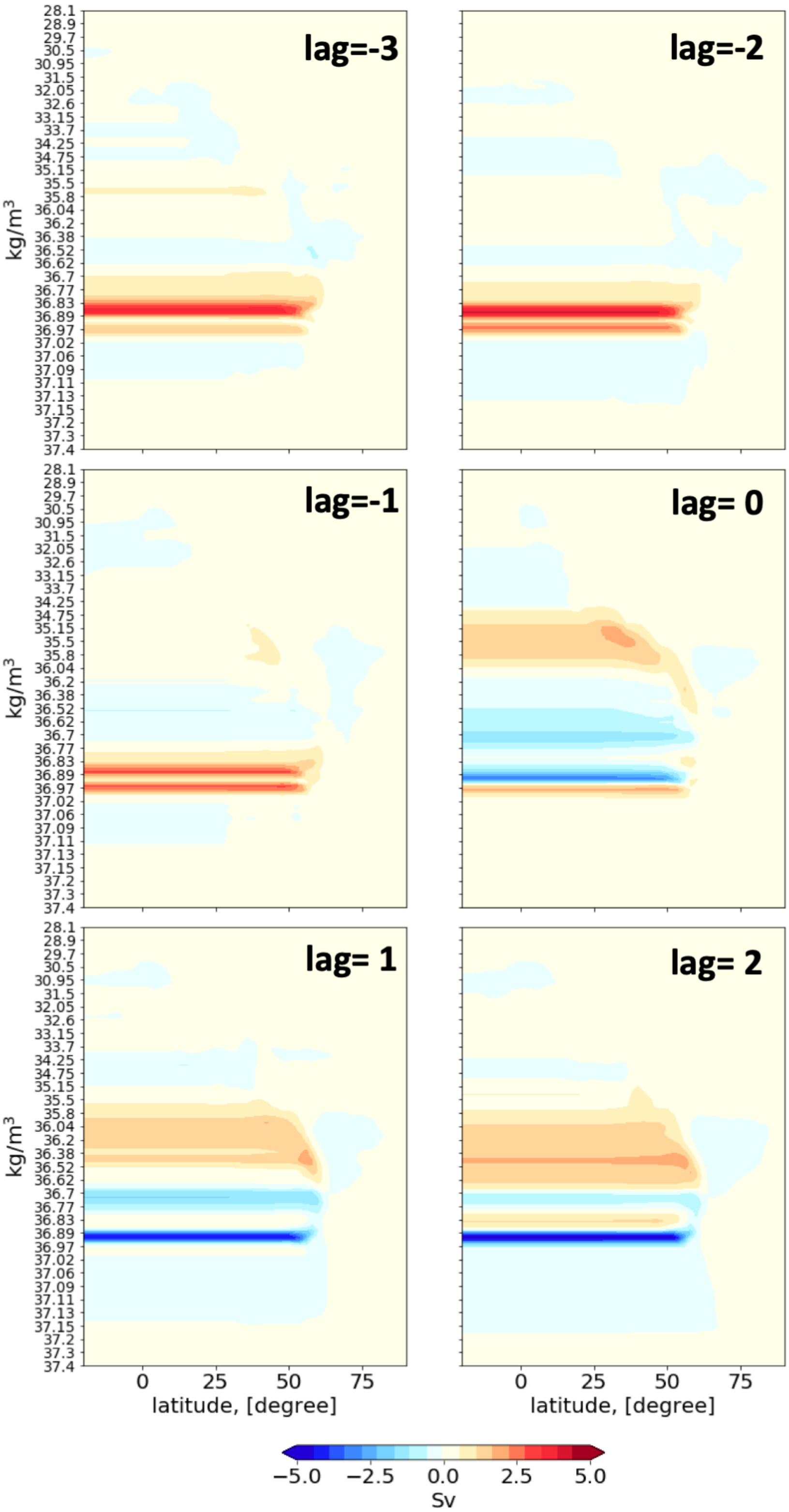

Figure 6: Differences between subpolar ϱ-AMOC$^+$ and ϱ-AMOC$^-$ composite patterns of surface-buoyancy-forced transformations (Ψ_s) shown at different lags (negative lag means Ψ_s is leading).

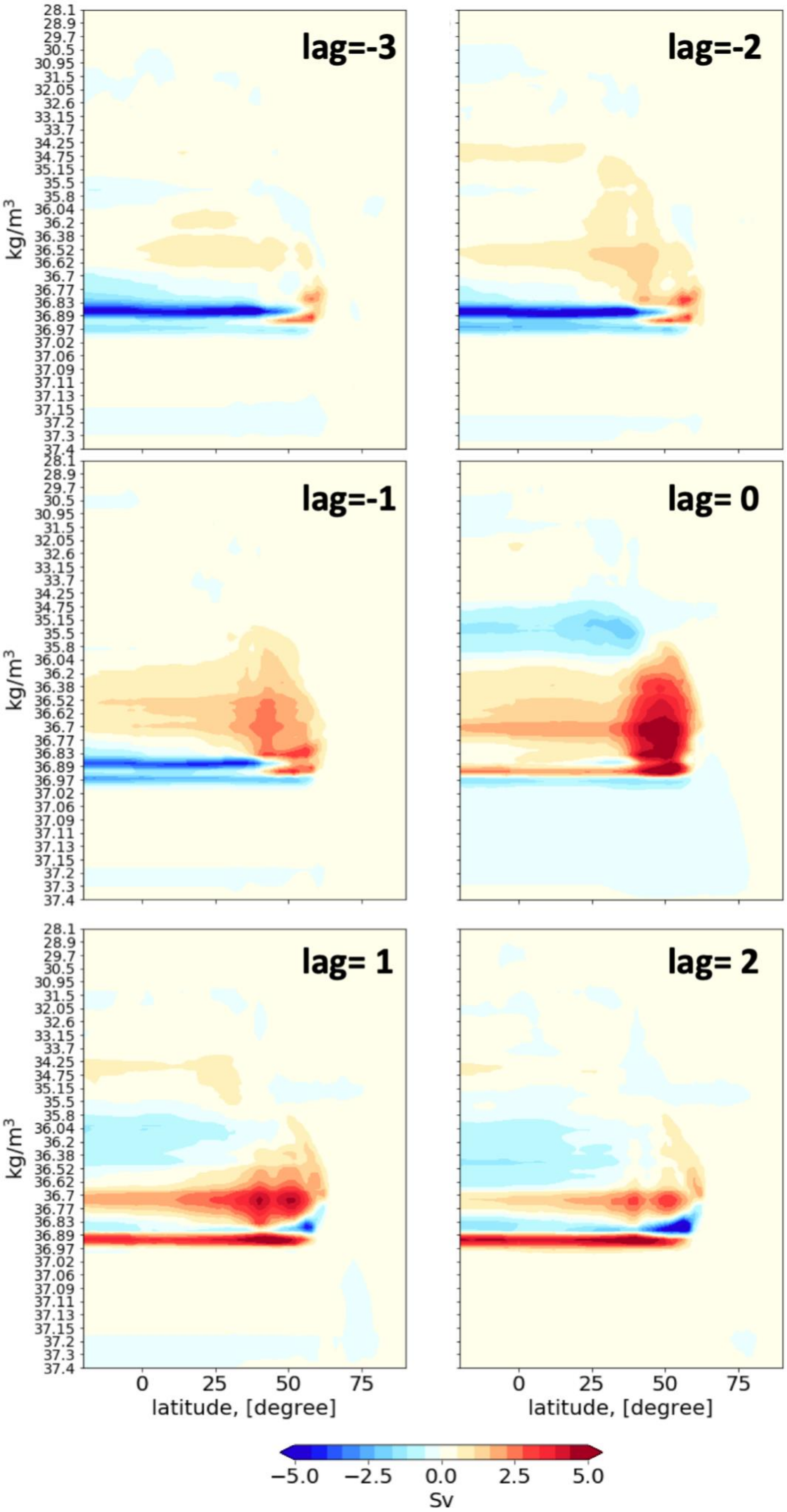

Figure 7: Same as Fig. 6 but for interior-mixing-induced transformations (Ψ_I).

4.3 Composites for vertical transport and diapycnal transformations

Composite patterns of vertical velocity at 1000 m during subpolar z-AMOC$^+$, z-AMOC$^-$, and the difference between both are presented in Fig. 8. Combining these patterns with the z-AMOC variability pattern (left panel of Fig. 5) we conclude that subpolar z-AMOC fluctuations are expressed by stronger sinking in the Gulf Stream and NAC regions, and stronger upwelling around Cape Hatteras during z-AMOC$^+$ as compared to z-AMOC$^-$. Interestingly, the difference between composites slightly changes sign along the NAC. It indicates that the z-AMOC variability might be partially linked to the shift in the position of the NAC. This in some way matches the findings by Frankignoul et al. 2013 who noticed a southward shift of the Gulf Stream during AMOC intensification.

As we have shown in section 4.2 the pattern of ϱ-AMOC variability is expressed by two cells centered at ϱ=36.7 kg m^{-3} and ϱ=36.89 kg m^{-3}. In Fig. 9 we present the ϱ-AMOC$^+$ and ϱ-AMOC$^-$ composite maps of diapycnal velocities and their differences across these two density levels. The variability of the upper cell in ϱ-AMOC (positive pattern in Fig. 5, right panel) is associated with the westward shift in the position of buoyancy loss in the Irminger Sea and more buoyancy loss at the southern tip of Greenland during ϱ-AMOC$^+$ as compared to ϱ-AMOC$^-$. This cell largely recirculates and is closed by more buoyancy gain along the NAC. The variability of the lower ϱ-AMOC cell (negative pattern in Fig. 5, right panel) is associated with the dipole anomaly of reduction of the buoyancy gain at the southern tip of Greenland and the reduction in buoyancy loss in the southern Labrador Sea (LS) and along the NAC during ϱ-AMOC$^+$. The reduction in buoyancy loss in the southern Labrador Sea and along the NAC during ϱ-AMOC$^+$ is dominant. Hence the lower cell of ϱ-AMOC variability spreads further south. In section 5 we speculate that this large latitudinal spread can be partially linked to the isopycnal motion which is spuriously imprinted as diapycnal transformation in the analysis.

Interior diapycnal velocities, inducing AMOC cells, redistribute the surface transformations which happen in succession through all density classes (at all levels). Hence, in Fig. 10 we present the mean surface transformations at two centers of the ϱ-AMOC pattern. At ϱ=36.7 kg m^{-3}, it is expressed by buoyancy gain and loss occurring at different locations. Buoyancy gain is found along the East Greenland Current (EGC) and Labrador Coastal Currents (LCC). It is primarily driven by the freshwater contribution to buoyancy flux (not shown). Concurrently, buoyancy loss occurs east of the buoyancy gain in the Irminger Sea, south of Iceland, in the Norwegian Sea and to a lesser degree in the Greenland Sea. Heat flux (not shown) is the main contributor to buoyancy change in these regions. At ϱ=36.89 kg m^{-3} the surface transformation is mainly expressed by buoyancy loss in the entire LS, in the Norwegian Sea and to a lesser degree in the Greenland Sea. Buoyancy gain is found only in the narrow area of the Denmark Strait. As one would expect, the map of mean surface transformations indicates that the LS is largely responsible for the deep water formation in the North Atlantic.

The differences between composites of surface transformations are presented in Fig. 11 for different lags. At ϱ=36.7 kg m^{-3} they indicate only minor anomalies in the LS before lag 0 which indicates that mainly the higher densities are exposed to the surface there. After the ϱ-AMOC reaches its maximum, lower densities are found along the periphery of the LS and the EGC and negative buoyancy anomalies start to appear at these locations. Concurrently, positive buoyancy anomalies are found in the Irminger Current and south of Iceland. Change in the heat flux is the prime driver for these anomalies. Interestingly, a similar pattern is also found in the composites for diapycnal velocities.

A different behaviour is seen at ϱ=36.89 kg m^{-3}. There, for negative lags we observe a northward shift of the buoyancy loss in the LS which is expressed by large negative buoyancy anomalies in the northern LS and less pronounced positive buoyancy anomalies in the southern LS. At lags 0 and later the patterns change the sign and mainly positive buoyancy anomalies are found along the periphery of the LS. Negative anomalies, however, still exist in the central LS and explain the appearance of the dipole pattern in □Ψ_s centered around ϱ=36.89 kg m^{-3} (see Fig.6 for positive lags).

Note that the anomaly of buoyancy gain at ϱ=36.89 kg m^{-3} and lower densities as imposed by the surface transformations at lags above or equal 0 may contribute to buoyancy loss at the lighter density classes in the presence of ‘upward’ internal diapycnal transformation. Upward diapycnal velocities at ϱ=36.89 kg m^{-3} are persistently present at the southern tip of Greenland (see bottom left and middle panels in Fig. 9). The importance of buoyancy loss contribution into the mid densities from the lower densities was already addressed in the analysis of the LS mean transformations (e.g., Xu et al. 2018, Sidorenko et al. 2020a). Here we speculate that this process is also associated with the variability of the AMOC.

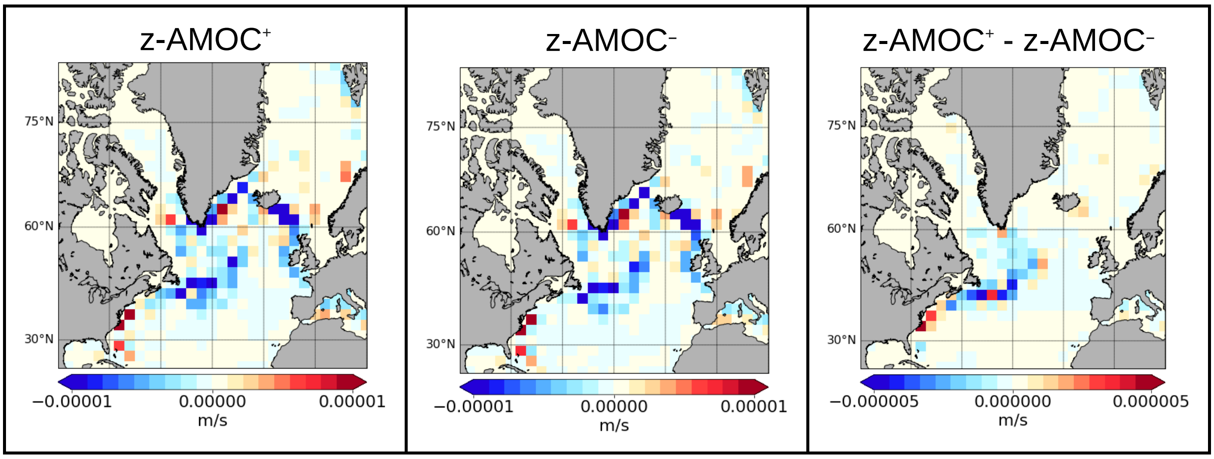

Figure 8: Composite maps of vertical velocity at 1000m during subpolar z-AMOC$^+$, z-AMOC$^-$, and their differences.

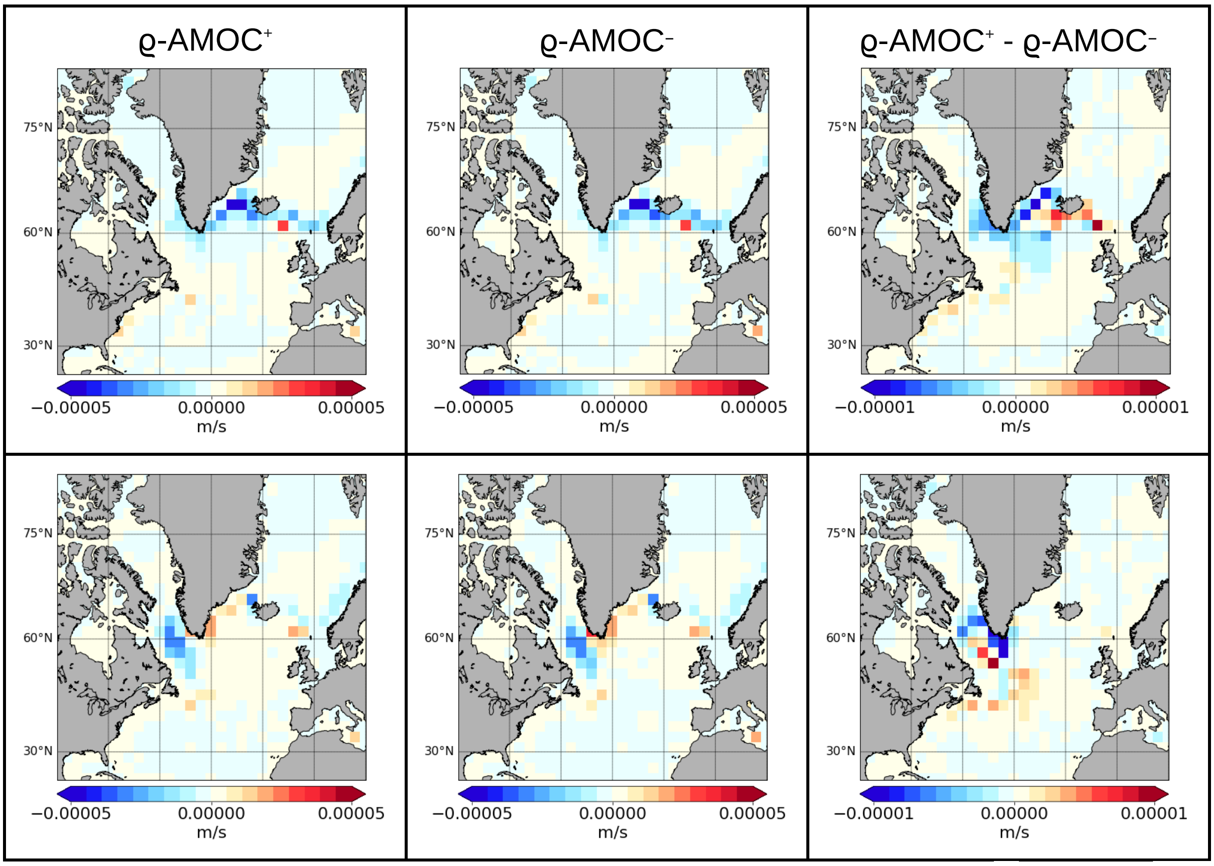

Figure 9: Composite maps of diapycnal velocity during ϱ-AMOC$^+$, ϱ-AMOC$^-$ and their differences shown for ϱ=36.7 kg/m^3 (upper panel) and ϱ=36.89 kg/m^3 (lower panel).

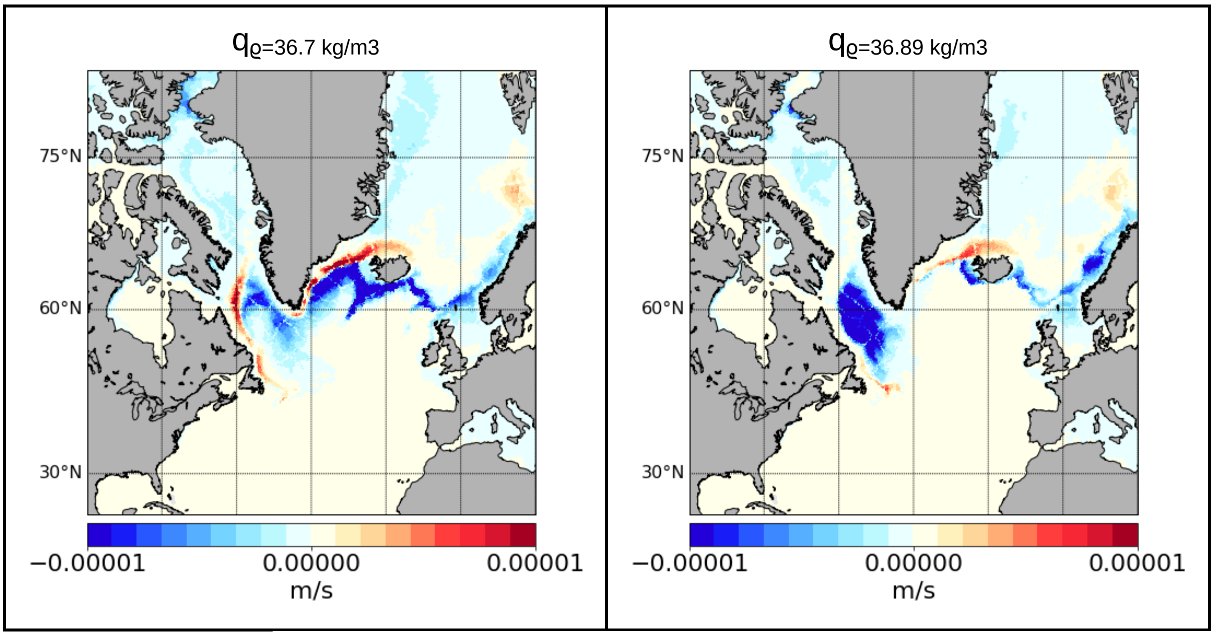

Figure 10: Mean surface-forced diapycnal water mass transformations per unit area across ϱ=36.7 kg/m^3 (left panel) and ϱ=36.89 kg/m^3 (right panel).

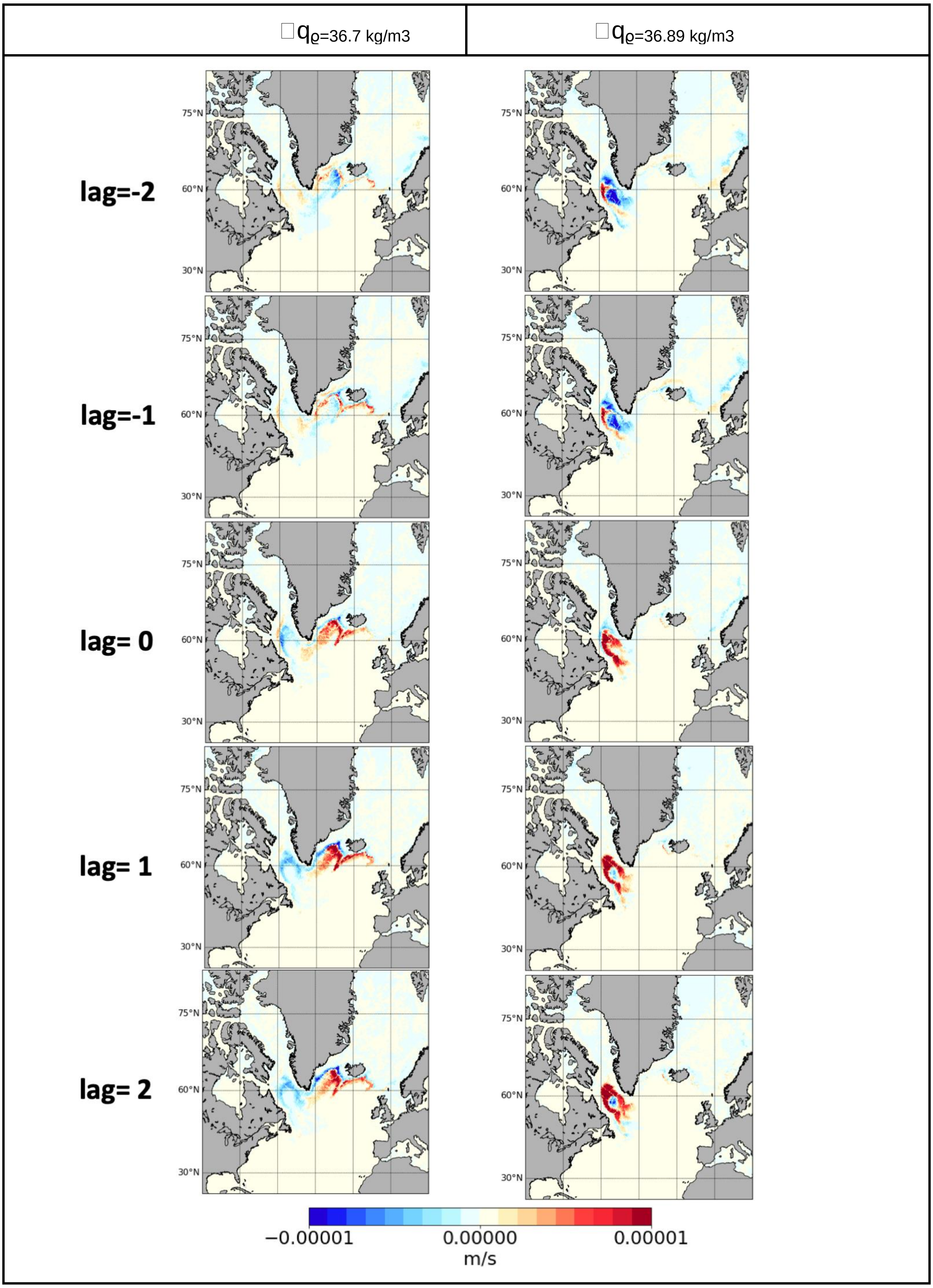

Figure 11: Differences between ϱ-AMOC$^+$ and ϱ-AMOC$^-$ composite patterns of surface buoyancy forced transformations for ϱ=36.7 kg/m^3 (left panel) and ϱ=36.89 kg/m^3 (right panel) shown for different lags. Negative lag means transformations lead.

4.4 AMOC relation to Sea Level Pressure and Mixed Layer Depth

Variability of the AMOC has been shown to be related to atmospheric forcing and to changes in deep-water formation (*e.g., Frankignoul et al. 2013, Menary et al. 2020b*). Here we analyse these links in our simulation. The maps of mean atmospheric Sea Level Pressure (SLP) and Mixed Layer Depth (MLD) maximum for the northern winter (JFM) are shown in Fig. 12 and resemble well-known patterns. In SLP the Azores high and Iceland low pressure centers are located at ~30°N and ~60°N, with an averaged pressure difference of ~30 hPa between both centers. The MLD pattern points to strong diapycnal mixing broadly along the NAC and Irminger Current regions, and in particular in the LS. Some mixing is also found in the Norwegian and Greenland Seas.

In Fig. 13 we present the differences between $AMOC^+$ and $AMOC^-$ composites of SLP at different lags for the two frameworks. Most of the SLP difference patterns resemble the North Atlantic Oscillation (NAO) variability pattern. As one would expect, a positive NAO phase (negative SLP anomalies around Iceland, positive SLP anomalies around the Azores) precedes the appearance of the AMOC maxima. In the z framework the positive NAO pattern is most expressed at lag=-3 but nearly vanishes at lag=-1. In contrast, in ϱ framework the pattern occurs at all negative lags, in particular at lag=-2. Differently lagged SLP anomaly patterns possibly reflects the fact that the AMOC maxima are found at different locations in the two frameworks and that it takes more time for the z-AMOC signal to travel from the area of deep convection to the location of the z-AMOC maximum at ~40°N. For ϱ-AMOC the behaviour is more coherent since the position of the maximum is found at ~55°N where the convection sites are. Interestingly, the two frameworks show distinct behaviour at lag 0, depicting large SLP increase centered at ~40°N in z framework, similar to a (northward-shifted) positive NAO, and at ~60°N in ϱ framework, similar to a (northward-shifted) negative NAO.

Differences between composites for MLD are shown in Fig. 14. It is worth noting that both frameworks exhibit large similarity which persists for positive and negative lags of several years. This highlights that the MLD variability is associated with a longer than year-to-year timescale. Noticeably, negative lags are associated with a northward shift of the MLD in the LS and positive lags with a southward shift. Hence, extensive deep water production in the northern part of the LS and the reduction of this in the southern LS precedes the appearance of AMOC maxima. This behaviour agrees with the differences in composites for the surface buoyancy flux across $\varrho=36.89\ kg/m^3$, representative for the deep water formation (right panel in Fig. 11).

In summary we find that at negative lags, the NAO-like patterns can be directly explained by their influence on buoyancy fluxes, with expected consequences for AMOC in both frameworks. Due to the large memory of the ocean state (we refer to

MLD here), several preceding years of positive NAO anomaly continually contribute to the AMOC increase. In contrast, at lag 0 the dominant impact is caused by the instantaneous Ekman transport: for z-AMOC the lag-0 SLP pattern is associated with easterly winds (Ekman transport to the north) anywhere south of ~45°N (where the high-pressure center is located), and for ϱ-AMOC the lag-0 SLP pattern is associated with easterly winds (Ekman transport to the north) anywhere between ~65°N (where the high pressure center is located) and ~40°N (where the low-pressure center is located). Our findings match those by *Ortega et at. 2012* who attributed high frequencies to local changes in Ekman transport caused by atmospheric modes of variability, and the low frequencies to the deep water production south of Greenland.

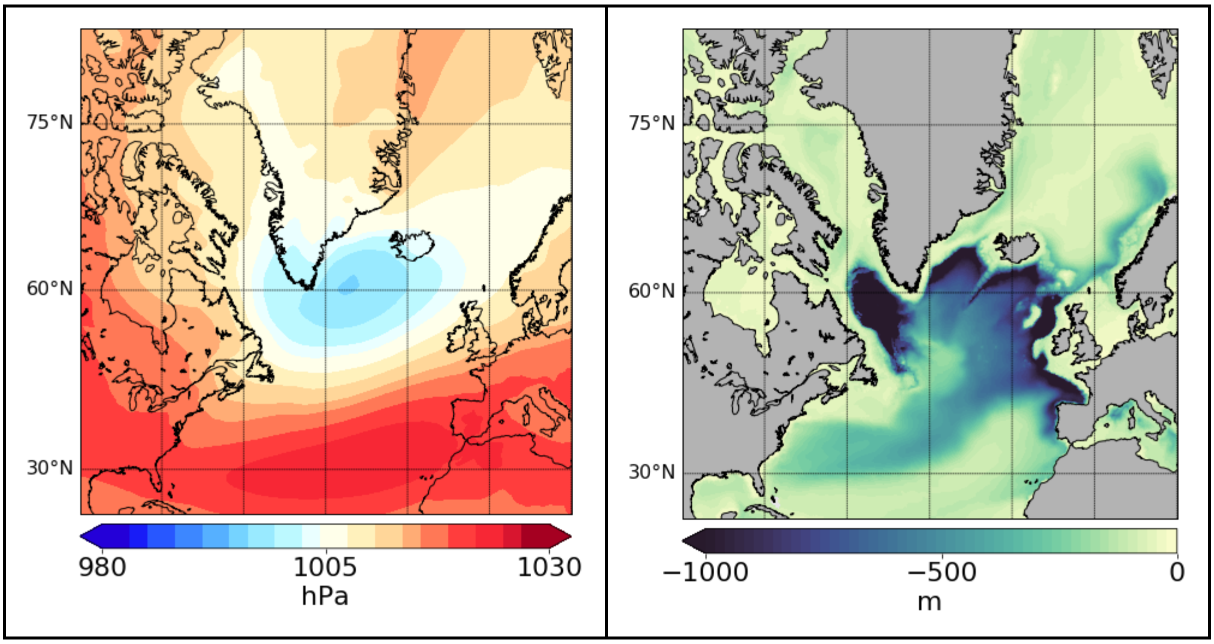

Figure 12: Maps of JFM mean Sea Level Pressure and the Mixed Layer Depth maximum. The means have been computed based on the last 900 years of the simulation.

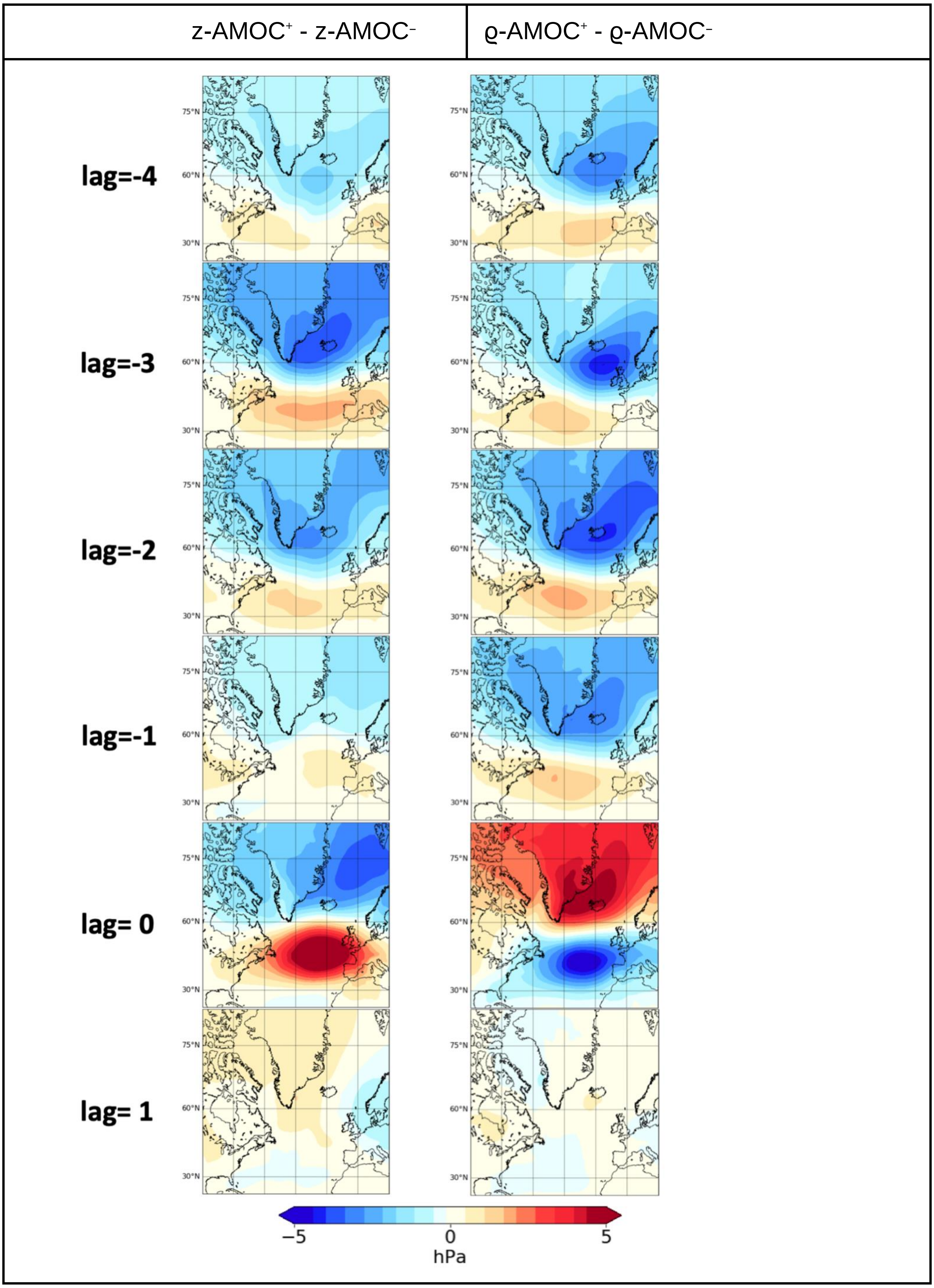

Figure 13: Differences between composites of SLP (JFM) for the subpolar z-AMOC index (left) and ϱ-AMOC index (right) for different lags (in years). Negative lag means SLP leads.

z-AMOC^{+} - z-AMOC^{-}	ϱ-AMOC^{+} - ϱ-AMOC^{-}

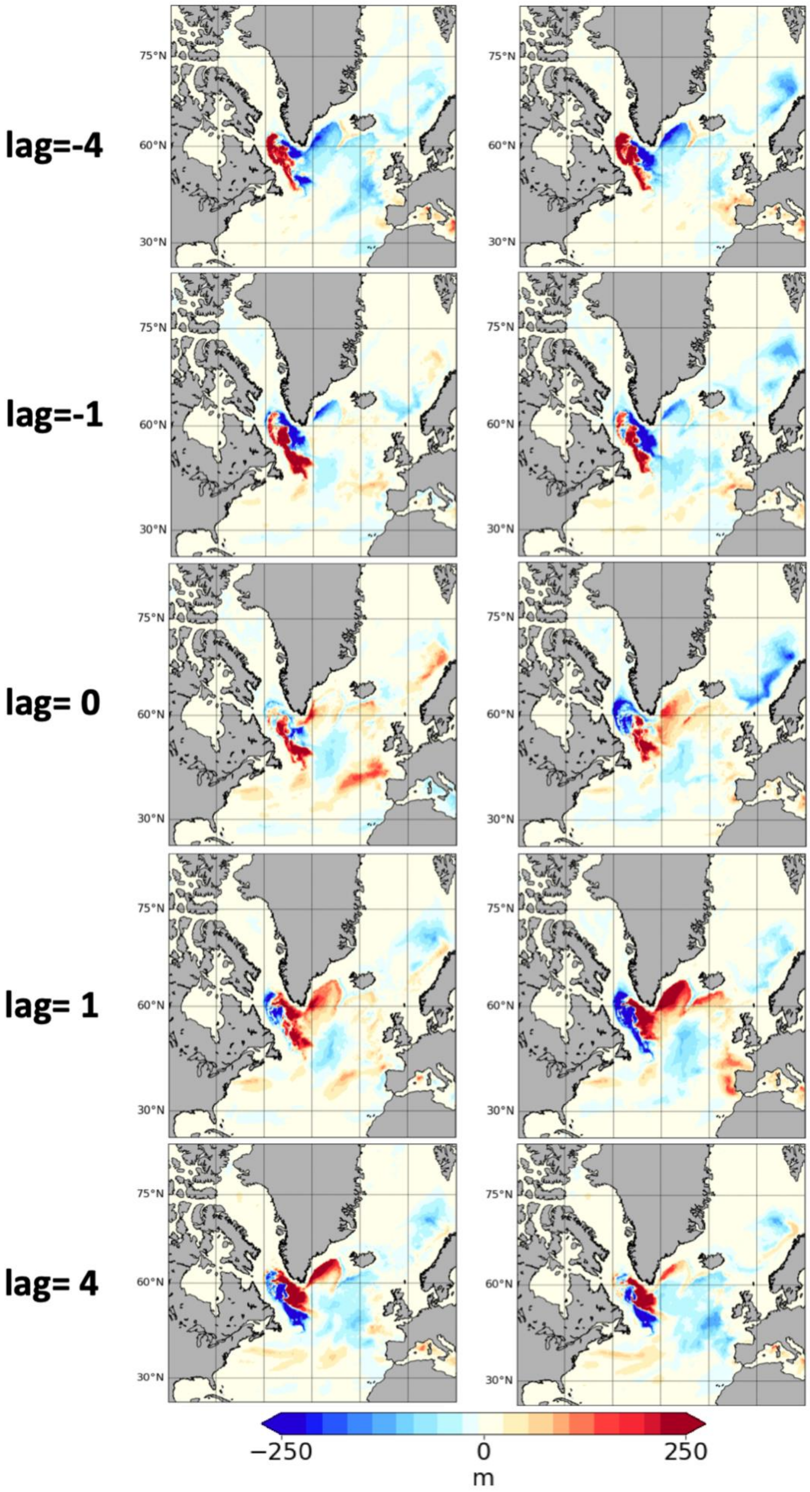

Figure 14: same as Figure12 but for MLD.

5. Discussion

The present study aims at illustrating the usability of augmenting the depth and density frameworks with the spatial patterns of sinking and diapycnal transformations for studying the AMOC and its variability. We analysed these patterns and their variability at a depth level (for z-AMOC) and at an isopycnal surface (for ϱ-AMOC) where AMOC reaches its maximum. The analysis requires horizontal binning, especially for vertical velocities which are too noisy in the main regions of up- and downwelling because of stepwise bottom topography. Conservative remapping to 4° x 4° boxes appeared optimal; finer bins still showed a rather patchy structure in regions with steep bathymetry. After the remapping step the main areas of sinking and upwelling, which constitute the AMOC, could be clearly identified. In contrast, the diapycnal velocities are less noisy and could be remapped to the finer meshes, but we still chose 4° x 4° boxes to ensure consistency. Depending on the purpose, remapping could be designed in a more elaborate way, for example by splitting the domain into geographical areas for illustrating their relative roles. The only trivial requirement here is that it should be conservative.

Since the present study was initially meant for AMOC and not transformation analysis, we did not store the model volume drift under isopycnals (the rate of volume change $\Delta V/\Delta t$ above the ϱ surface) as discussed in 4.2. Thus, the internal transformations which we present in Fig. 7 are biased by these adiabatic fluctuations. For the long-term averages used in this paper, this drift is negligible and therefore does not change the mean transformation fields. However, it may bias patterns of their variability. Hence we speculate that the large-scale latitudinal spread of the bottom cell of variability seen in Fig. 5 (right panel, bottom negative cell) as well as in Fig.7 (basinwide stripes in the high density classes) can be caused by adiabatic fluctuations. It is also worth noting that internal transformations redistribute the surface buoyancy fluxes which have been aggregated over some period of time and the partition of □Ψ_{ϱ} onto □Ψ_{s} and □Ψ_{I} becomes (due to possible lags) less apparent if made instantaneously or on a year-to-year basis. Although this partitioning works for mean fields, some deeper look into consistent ways for partitioning the anomalies is required.

It is known that more insight can be gained from the AMOC analysis in density framework as it allows one to distinguish between surface-buoyancy-forced and internal transformations (*e.g., Zhang et al. 2010, Xu et al. 2018, Sidorenko et al. 2020a*). Our deeper analysis in the density framework reveals that looking at spatial patterns of transformations only at the locations where AMOC reaches its maximum may be sufficient to learn about the mean AMOC, but is insufficient to address its variability. Indeed, the places where transformations through selected isopycnals are large do not imply that the ϱ-AMOC is being modified right there. Surface transformations happen in succession through all density classes (at all levels) and are further redistributed by interior diapycnal transformations. Hence, for addressing the AMOC variability we augmented the composite maps of ϱ-AMOC and its constituents at different isopycnal levels. Only the aggregated analysis allows one to associate deep-water production with AMOC changes.

We note that subpolar AMOC maxima in both frameworks are located at different latitudes and hence not only differ in mechanisms of underlying sinking and diapycnal transformations but also disagree on temporal delays. Although the latitudinal propagation of AMOC perturbation signals might be of high interest, it is known to be prone to errors due to model uncertainties and resolution (e.g., Frankignoul et al. 2013, Katsman et al., 2018; Menary & Hermanson, 2018; Menary et al. 2020a). We plan to analyze latitudinal propagation of AMOC-related anomalies in future work by employing an eddy-resolving setup of the North Atlantic.

6. Conclusions

We analyzed the AMOC variability in a 900 years climate run by using density and z frameworks. The AMOC variability is nearly identical in both frameworks south of ~30°N where the isopycnals are nearly flat. In the northern North Atlantic, where isopycnals are sloping, the two frameworks show substantial differences. First, the recirculation cell and hence the maximum of the subpolar AMOC are located at different latitudes for the two frameworks. Second, the variability of the subpolar AMOC maxima is correlated with a coefficient of only ~0.4 on the annual timescale (0.64 after applying a 5-year moving average), implying that the associated patterns of variability (difference between composites) are different. The ϱ-AMOC emphasises the role of internal transformations.

The individual analysis of internally and surface-forced constituents of the AMOC reveals that variability is largely driven by internal transformations which are triggered by the surface buoyancy flux. Negative heat flux anomalies in the northern LS, reduced freshwater export from the Nordic Seas, and an associated northward shift of MLD there precedes AMOC maxima. Interestingly, AMOC maxima are followed by reversed anomalies.

Another interesting detail is that the upward diapycnal velocities along the path of the NAC, corresponding to the southern end of the mid-depth recirculation cell in ϱ-AMOC and related to its variability, occur in the absence of surface transformations in this area. Hence, as in *Sidorenko et al. 2020a*, we attribute this behaviour to spurious numerical mixing due to sloping isopycnals that essentially deviate from level surfaces.

We found that the surface buoyancy transformations which precede AMOC maxima are associated with NAO-like SLP anomaly patterns. Furthermore, a more coherent response to atmospheric change is found in the density framework rather than in z. Yet, at the year with high AMOC the dominant impact in both frameworks is caused by the instantaneous Ekman transport. Given that no association between SLP and AMOC is found at positive lags (AMOC leads), we conclude that the atmosphere is the main driver for AMOC anomalies rather than the other way around. In contrast, the MLD anomaly is linked with AMOC for both negative and positive lags, pointing to the long-term ocean memory.

Acknowledgments

The work was supported by the Helmholtz Climate Initiative REKLIM (Regional Climate Change) (Q. Wang, D. Sidorenko), the APPLICATE (Advanced Prediction in Polar regions and beyond: modelling, observing system design and LInkages associated with a Changing Arctic climaTE, grant number H2020-BG-2016-1) (T. Jung), contribution to the projects S1, S2 and L4 of the Collaborative Research Centre TRR 181 "Energy Transfer in Atmosphere and Ocean" funded by the Deutsche Forschungsgemeinschaft (DFG, German Research Foundation) under project number 274762653 (S. Danilov, J. Streffing, S. Juricke, N. Koldunov, P. Scholz), the EC Horizon 2020 project PRIMAVERA under the grant agreement no. 641727, the state assignment of FASO Russia theme No. 0149-2019-0015 (D. Sein), and the Federal Ministry of Education and Research of Germany (BMBF) in the framework of SSIP, grant 01LN1701A (H. Goessling). The authors gratefully acknowledge the Earth System Modelling Project (ESM) for funding this work by providing computing time on the ESM partition of the supercomputer JUWELS at the Jülich Supercomputing Centre (JSC).

Data Availability

Datasets related to this article can be found at:
https://swiftbrowser.dkrz.de/tcl_s/VAimsi4XJbaOm6

References

Buckley, M. W. and Marshall, J. (2016), Observations, inferences, and mechanisms of the Atlantic Meridional Overturning Circulation: A review, *Rev. Geophys.*, 54, doi:10.1002/2015RG000493.

Cunningham, S. A., Kanzow, T., Rayner, D., Baringer, M. O., Johns, W. E., Marotzke, J., ... & Meinen, C. S. (2007). Temporal variability of the Atlantic meridional overturning circulation at 26.5 N. *science*, *317*(5840), 935-938, doi:10.1126/science.1141304

Danabasoglu, Gokhan, Steve G. Yeager, Young-Oh Kwon, Joseph J. Tribbia, Adam S. Phillips, and James W. Hurrell. " Variability of the Atlantic Meridional Overturning Circulation in CCSM4", *Journal of Climate* 25, 15 (2012): 5153-5172, accessed Mar 23, 2021, https://doi.org/10.1175/JCLI-D-11-00463.1

Danabasoglu, G., S. G. Yeager, W. M. Kim, E. Behrens, M. Bentsen, D. Bi, A. Biastoch, R. Bleck, C. Böning, A. Bozec, V. M. Canuto, C. Cassou, E. Chassignet, A. C. Coward, S. Danilov, N. Diansky, H. Drange, R. Farneti, E. Fernandez, P. G. Fogli, G. Forget, Y. Fujii, S. M. Griffies, A. Gusev, P. Heimbach, A. Howard, M. Ilicak, T. Jung, A. R. Karspeck, M. Kelley, W. G. Large, A. Leboissetier, J. Lu, G. Madec, S. J. Marsland, S. Masina, A. Navarra, A. J. G. Nurser, A. Pirani, A. Romanou, D. Salas y Melia, B. L. Samuels, M. Scheinert, D. Sidorenko, S. Sun, A.-M. Treguier, H. Tsujino, P. Uotila, S. Valcke, A. Voldoire, Q. Wang, and I. Yashayaev, 2016: North Atlantic simulations in Coordinated Ocean-ice Reference Experiments phase II (CORE-II). Part II: Inter-annual to decadal variability. Ocean Modelling, 97, 65-90, doi: 10.1016/j.ocemod.2015.11.007.

Danilov, S., Kivman, G., & Schröter, J. (2004). A finite-element ocean model: principles and evaluation. Ocean Modelling, 6(2), 125-150, 10.1016/S1463-5003(02)00063-X

Danilov, S., Sidorenko, D., Wang, Q. and Jung, T., 2017: The Finite-volumE Sea ice–Ocean Model (FESOM2), Geoscientific Model Development, 10(2), 765–789, doi:10.5194/gmd-10-765-2017.

Danilov, S., Wang, Q., Timmermann, R., Iakovlev, N., Sidorenko, D., Kimmritz, M., Jung, T., and Schröter, J.: Finite-Element Sea Ice Model (FESIM), version 2, Geosci. Model Dev., 8, 1747-1761, doi.org/10.5194/gmd-8-1747-2015, 2015.

Frankignoul, Claude, Guillaume Gastineau, and Young-Oh Kwon. " The Influence of the AMOC Variability on the Atmosphere in CCSM3", *Journal of Climate* 26, 24 (2013): 9774-9790, accessed Mar 23, 2021, https://doi.org/10.1175/JCLI-D-12-00862.1

G. Forget, Y. Fujii, S. M. Griffies, A. Gusev, P. Heimbach, A. Howard, M. Ilicak, T. Jung, A. R. Karspeck, M. Kelley, W. G. Large, A. Leboissetier, J. Lu, G. Madec, S. J. Marsland, S. Masina, A. Navarra, A. J. G. Nurser, A. Pirani, A. Romanou, D. Salas y Melia, B. L. Samuels, M. Scheinert, D. Sidorenko, S. Sun, A.-M. Treguier, H. Tsujino, P. Uotila, S. Valcke, A. Voldoire, Q. Wang, and I. Yashayaev, 2016: North Atlantic simulations in Coordinated Ocean-ice Reference Experiments phase II (CORE-II). Part II: Inter-annual to decadal variability. Ocean Modelling, 97, 65-90, doi: 10.1016/j.ocemod.2015.11.007

Johnson, H. L., Cessi, P., Marshall, D. P., Schloesser, F., & Spall, M. A. (2019). Recent contributions of theory to our understanding of the Atlantic Meridional Overturning Circulation. Journal of Geophysical Research: Oceans, 124, 5376–5399, doi:10.1029/2019JC015330

Hirschi, J. J.- M., Barnier, B., Böning, C., Biastoch, A., Blaker, A. T., Coward, A., et al. (2020). The Atlantic meridional overturning circulation in high resolution models. Journal of Geophysical Research: Oceans, 125, doi:10.1029/2019JC015522

Katsman, C. A., Drijfhout, S. S., Dijkstra, H. A., & Spall, M. A. (2018). Sinking of dense North Atlantic waters in a global ocean model: Location and controls. Journal of Geophysical Research: Oceans, 123. doi:10.1029/ 2017JC013329
Kwon, Y., and C. Frankignoul, 2014: Mechanisms of Multidecadal Atlantic Meridional Overturning Circulation Variability Diagnosed in Depth versus Density Space. J. Climate, 27, 9359–9376, https://doi.org/10.1175/JCLI-D-14-00228.1.

Kuhlbrodt, T., Griesel, A., Montoya, M., Levermann, A., Hofmann, M., and Rahmstorf, S. (2007), On the driving processes of the Atlantic meridional overturning circulation, Rev. Geophys., 45, RG2001, doi:10.1029/2004RG000166.

Kwon, Young-Oh, and Claude Frankignoul. " Mechanisms of Multidecadal Atlantic Meridional Overturning Circulation Variability Diagnosed in Depth versus Density Space", *Journal of Climate* 27, 24 (2014): 9359-9376, accessed Mar 23, 2021, https://doi.org/10.1175/JCLI-D-14-00228.1

Lozier, M. S. and Li, F. and Bacon, S. and Bahr, F. and Bower, A. S. and Cunningham, S. A. and de Jong, M. F. and de Steur, L. and deYoung, B. and Fischer, J. and Gary, S. F. and Greenan, B. J. W. and Holliday, N. P. and Houk, A. and Houpert, L. and Inall, M. E. and Johns, W. E. and Johnson, H. L. and Johnson, C. and Karstensen, J. and Koman, G. and Le Bras, I. A. and Lin, X. and Mackay, N. and Marshall, D. P. and Mercier, H. and Oltmanns, M. and Pickart, R. S. and Ramsey, A. L. and Rayner, D. and Straneo, F. and Thierry, V. and Torres, D. J. and Williams, R. G. and Wilson, C. and Yang, J. and Yashayaev, I. and Zhao, J. 2019. A sea change in our view of overturning in the subpolar North Atlantic. Science, 516-521, doi:10.1126/science.aau6592

Megann, A. (2018). Estimating the numerical diapycnal mixing in an eddy-permitting ocean model. *Ocean Modelling*, *121*, 19-33. doi:10.1016/j.ocemod.2017.11.001

Menary, M. B., Roberts, C. D., Palmer, M. D., Halloran, P. R., Jackson, L., Wood, R. A., Müller, W. A., Matei, D., and Lee, S.- K. (2013), Mechanisms of aerosol- forced AMOC variability in a state of the art climate model, *J. Geophys. Res. Oceans*, 118, 2087– 2096, doi:10.1002/jgrc.20178.

Menary, M.B., Hermanson, L. Limits on determining the skill of North Atlantic Ocean decadal predictions. *Nat Commun* 9, 1694 (2018). https://doi.org/10.1038/s41467-018-04043-9

Menary, M. B., Robson, J., Allan, R. P., Booth, B. B. B., Cassou, C., & Gastineau, G., et al. (2020a). Aerosol- forced AMOC changes in CMIP6 historical simulations. *Geophysical Research Letters*, 47, e2020GL088166. https://doi.org/10.1029/2020GL088166

Menary, M. B., Jackson, L. C., & Lozier, M. S. (2020b). Reconciling the relationship between the AMOC and Labrador Sea in OSNAP observations and climate models. *Geophysical Research Letters*, 47, e2020GL089793. https://doi.org/10.1029/2020GL089793

Oelsmann, J., Borchert, L., Hand, R., Baehr, J., & Jungclaus, J. H. (2020). Linking ocean forcing and atmospheric interactions to Atlantic multidecadal variability in MPI- ESM1.2. *Geophysical Research Letters*, 47, e2020GL087259. https://doi.org/10.1029/2020GL087259

Ortega, P., Montoya, M., González-Rouco, F. *et al.* Variability of the Atlantic meridional overturning circulation in the last millennium and two IPCC scenarios. *Clim Dyn* 38, 1925–1947 (2012). https://doi.org/10.1007/s00382-011-1081-6

Rackow, T. and co-authors (2016), Towards multi-resolution global climate modeling with ECHAM6-FESOM. Part II: climate variability, Clim. Dyn. doi:10.1007/s00382-016-3192-6

Roberts, C. D., et al. (2013), Atmosphere drives recent interannual variability of the Atlantic meridional overturning circulation at 26.5°N, *Geophys. Res. Lett.*, 40, 5164– 5170 doi:10.1002/grl.50930.

Reintges, A., Martin, T., Latif, M. *et al.* Uncertainty in twenty-first century projections of the Atlantic Meridional Overturning Circulation in CMIP3 and CMIP5 models. *Clim Dyn*49, 1495–1511 (2017). https://doi.org/10.1007/s00382-016-3180-x

Scholz, P., Sidorenko, D., Gurses, O., Danilov, S., Koldunov, N., Wang, Q., ... & Jung, T. (2019). Assessment of the Finite-volumE Sea ice-Ocean Model (FESOM2. 0)–Part 1: Description of selected key model elements and comparison to its predecessor version. *Geoscientific Model Development*, *12*(11). doi:10.5194/gmd-12-4875-2019

Sidorenko D. and co-authors (2015). Towards multi-resolution global climate modeling with ECHAM6–FESOM. Part I: model formulation and mean climate, Climate Dynamics, doi:10.1007/s00382-014-2290-6

Sidorenko, D., Goessling, H. F., Koldunov, N. V., Scholz, P., Danilov, S., Barbi, D., et al (2019). Evaluation of FESOM2.0 coupled to ECHAM6.3: Pre- industrial and HighResMIP simulations. Journal of Advances in Modeling Earth Systems, 11. doi.org/10.1029/2019MS001696

Sidorenko, D., Danilov, S., Koldunov, N., Scholz, P., and Wang, Q.: Simple algorithms to compute meridional overturning and barotropic streamfunctions on unstructured meshes, Geosci. Model Dev., 13, 3337–3345, https://doi.org/10.5194/gmd-13-3337-2020, 2020a.

Sidorenko, D., Danilov, S., Fofonova, V., Cabos, W., Koldunov, N., Scholz, P., et al. (2020b). AMOC, watermass transformations and their responses to changing resolution in the Finite- volumE Sea ice–Ocean Model. Journal of Advances in Modeling Earth Systems, 12, e2020MS002317. Accepted Author Manuscript. doi.org/10.1029/2020MS002317

Timmermann, R., Danilov, S., Schröter, J., Böning, C., Sidorenko, D., Rollenhagen, K. (2009). Ocean circulation and sea ice distribution in a finite element global sea ice–ocean model, Ocean Modelling, Volume 27, Issue 3, Pages 114-129, ISSN 1463-5003, dx.doi.org/10.1016/j.ocemod.2008.10.009.

Tsujino, H., Urakawa, L. S., Griffies, S. M., Danabasoglu, G., Adcroft, A. J., Amaral, A. E., Arsouze, T., Bentsen, M., Bernardello, R., Böning, C. W., Bozec, A., Chassignet, E. P., Danilov, S., Dussin, R., Exarchou, E., Fogli, P. G., Fox-Kemper, B., Guo, C., Ilicak, M., Iovino, D., Kim, W. M., Koldunov, N., Lapin, V., Li, Y., Lin, P., Lindsay, K., Liu, H., Long, M. C., Komuro, Y., Marsland, S. J., Masina, S., Nummelin, A., Rieck, J. K., Ruprich-Robert, Y., Scheinert, M., Sicardi, V., Sidorenko, D., Suzuki, T., Tatebe, H., Wang, Q., Yeager, S. G., and Yu, Z. (2020). Evaluation of global ocean–sea-ice model simulations based on the experimental protocols of the Ocean Model Intercomparison Project phase 2 (OMIP-2), Geosci. Model Dev., https://doi.org/10.5194/gmd-2019-363, accepted.

Walin, G., 1982: On the relation between sea-surface heat flow and thermal circulation in the ocean. Tellus, 34, 187–195, https://doi.org/10.3402/tellusa.v34i2.10801

Wang, Q., Danilov, S., & Schröter, J. (2008). Finite element ocean circulation model based on triangular prismatic elements, with application in studying the effect of topography representation. Journal of Geophysical Research: Oceans, 113(C5). DOI: 10.1029/2007JC004482

Wang, Q., Danilov, S., Sidorenko, D., Timmermann, R., Wekerle, C., Wang, X., Jung, T., and Schröter, J., 2014: The Finite Element Sea Ice-Ocean Model (FESOM) v.1.4: formulation of an ocean general circulation model, Geosci. Model Dev., 7, 663–693, doi:10.5194/gmd-7-663-2014

Xu, X., P.B. Rhines, and E.P. Chassignet, 2018: On Mapping the Diapycnal Water Mass Transformation of the Upper North Atlantic Ocean. J. Phys. Oceanogr., 48, 2233–2258, doi:10.1175/JPO-D-17-0223.1

Xu, X., Chassignet, E.P. & Wang, F. On the variability of the Atlantic meridional overturning circulation transports in coupled CMIP5 simulations. *Clim Dyn* 52, 6511–6531 (2019). https://doi.org/10.1007/s00382-018-4529-0

Wang, Q., Ilicak, M., Gerdes, R., Drange, H., Aksenov, Y., Bailey, D. A., . . . Yeager, S. G. (2016a). An assessment of the Arctic Ocean in a suite of interannual CORE-II simulations. Part II: Liquid freshwater. Ocean Modelling, 99, 86-109. doi: 10.1016/j.ocemod.2015.12.009

Wang, Q., Ilicak, M., Gerdes, R., Drange, H., Aksenov, Y., Bailey, D. A., . . . Yeager, S. G. (2016b). An assessment of the Arctic Ocean in a suite of interannual CORE-II simulations. Part I: Sea ice and solid freshwater. Ocean Modelling, 99, 110-132. doi: 10.1016/j.ocemod.2015.12.008

Zhang, R. (2010), Latitudinal dependence of Atlantic meridional overturning circulation (AMOC) variations, *Geophys. Res. Lett.*, 37, L16703, doi:10.1029/2010GL044474.